Journal of Colloid and Interface Science 604 (2021) 798–809

Contents lists available at ScienceDirect

Journal of Colloid and Interface Science

journal homepage: www.elsevier.com/locate/jcis

3D hollow Bi_2O_3@CoAl-LDHs direct Z-scheme heterostructure for visible-light-driven photocatalytic ammonia synthesis

Shengjie Xia [a,*], Guanhua Zhang [a], Zhiyan Gao [a], Yue Meng [b,c], Bo Xie [a], Hanfeng Lu [a], Zheming Ni [a]

[a] Department of Chemistry, College of Chemical Engineering, Zhejiang University of Technology, 18 Chaowang Road, Hangzhou 310014, PR China
[b] School of Life Science, Huzhou University, 759 East Erhuan Road, Huzhou 313000, PR China
[c] Department of Life and Health Sciences, Huzhou College, 313000 Huzhou, PR China

GRAPHICAL ABSTRACT

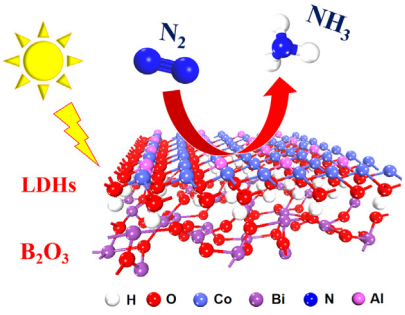

ARTICLE INFO

Article history:
Received 15 June 2021
Revised 5 July 2021
Accepted 11 July 2021
Available online 16 July 2021

Keywords:
3D structure core-shell
Bi_2O_3@CoAl-LDHs
Z-scheme heterojunction
Visible light
Photocatalytic ammonia synthesis

ABSTRACT

In this paper, the novel 3D hollow Z-scheme heterojunction photocatalysts based on Bi_2O_3 and CoAl layered double hydroxides (Bi_2O_3@CoAl-LDHs) were prepared for efficient visible-light-driven photocatalytic ammonia synthesis. The synthesized nanohybrid exhibits excellent photocatalytic ammonia synthesis performance (48.7 $\mu mol \cdot L^{-1} \cdot h^{-1}$) and structural stability, which is primarily attributed to the fact that Z-scheme heterojunction significantly enhanced lifetime of photogenerated carriers (6.22 ns) and transfer efficiency of surface photogenerated electrons (72.5%). Strict control experiments and nitrogen isotope labeling results show that nitrogen and hydrogen in the produced ammonia come from nitrogen and water in the reactant respectively. Electron paramagnetic resonance (EPR) experiments and density functional theory (DFT) calculations further reveal that the built-in electric field due to the difference between Bi_2O_3 and CoAl-LDHs is the key to constructing the Z-scheme heterojunction. In addition, results of partial density of states (PDOS) show that Co in Bi_2O_3@CoAl-LDHs composite is the active site for photocatalytic N_2 fixation.

1. Introduction

Ammonia (NH_3), as one of the most essential chemicals in the world, has been widely used in agriculture, chemical and pharmaceutical fields. In addition, liquid ammonia has a higher transportability and energy density than liquid H_2, which means that it also has a huge application potential in the field of fuel cells [1,2]. However, NH_3 production in industry mainly relies on Haber-Bosch process, which require conditions of high temperature (400–600 °C) and high pressure (20–40 MPa) with nitrogen and hydrogen as raw materials. More seriously, the annual energy consumption accounts for ~2% of the world's total energy and 300 million tons of CO_2 greenhouse gases are emitted in the Haber-Bosch process

* Corresponding author.
E-mail address: xiasj@zjut.edu.cn (S. Xia).

https://doi.org/10.1016/j.jcis.2021.07.063
0021-9797/

[3,4]. As the demand for NH_3 grows, green, sustainable and economical nitrogen fixation strategies are needed. In 1977, Schrauzer et al. [5] first discovered that the TiO_2-based photocatalysts can achieve nitrogen fixation under ultraviolet light. Since then, the photocatalytic nitrogen reduction reaction (NRR) is considered to be a potential alternative to the industrial Haber-Bosch process. Because the inexhaustible solar energy and water resources instead of fossil fuels and hydrogen are used as the active electrons and protons for nitrogen fixation in the photocatalytic NRR reaction [6]. However, the bottom of the conduction band of the photocatalysts must be higher than the potential of N_2 reduction (N_2/NH_3 = −0.0922 eV,N_2/NH_4^+ = 0.273 eV vs. NHE) in order to satisfy the thermodynamic conditions [7,8]. Therefore, the first problem that needs to be solved to achieve the photocatalytic NRR is to find a suitable photocatalyst.

In recent years, layered double hydroxides (LDHs) have gained heightened attention in photocatalytic nitrogen reduction reaction (pNRR) due to their unique structure and suitable energy band structure [9,10,11]. More importantly, the photogenerated electrons on the conduction band of LDHs have a strong reduction potential, which is conducive to the occurrence of the NRR reaction [12,13]. However, the low carrier transport rate and high carrier recombination greatly limit performance of pNRR [14]. Studies have shown that the construction of Z-scheme heterojunction inspired by natural photosynthesis can be an efficient method to mitigate the recombination of photo-generated carriers and promote the transportation of hot electrons [15,16]. The electron migration mechanism of Z-scheme heterojunction is shown in Fig. S1 [17,18]. The electrons on the conduction band (CB) of semiconductor B recombine with the holes on the valence band (VB) of semiconductor A, with the result that the photo-generated electrons are mainly enriched in the CB of semiconductor A and the holes are mainly enriched in the VB of semiconductor B. This special electron transfer path implements the efficient separation of photo-generated carriers in space, which exhibits stronger oxidation potential and reduction potential compared with the single photocatalyst and the traditional Type-II heterojunction [19]. Thus, the problem of photogenerated carrier recombination can be effectively solved by finding another semiconductor photocatalyst to construct a Z-scheme heterojunction.

Bismuth oxide (Bi_2O_3) is considered to be one of the extremely promising photocatalysts because of its low cost, non-toxicity, and strong light absorption properties [20,21]. However, the photocatalytic activity of pure Bi_2O_3 usually has slow electron transport speed and low photocatalytic performance, while it is preferable to fabricate the heterojunction photocatalysts, in which the hybridized semiconductor will efficiently separate the photogenerated electrons/holes to enhance its photocatalytic performance. It is worth noting that the band structure of Bi_2O_3 is very suitable for constructing Z-scheme heterojunctions, such as Bi_2O_3@CoO [22], Bi@Bi_2O_3/g-C_3N_4 [23], Bi_2S_3/Bi_2O_3/$ZnIn_2S_4$ [24]. Based on the above analysis, it can be inferred that the Z-scheme heterojunction photocatalyst constructed of LDHs and Bi_2O_3 may not only achieve the efficient separation of photo-generated electrons and holes, but also retain the more reductive photo-generated electrons for NRR.

In this paper, a novel 3D Bi_2O_3@CoAl-LDHs Z-scheme heterojunction photocatalysts with a core-shell structure were produced by in-situ growth method. The design of Bi_2O_3@CoAl-LDHs is ingenious: (1) Bi_2O_3 and LDHs nanosheets are contact to form a core-shell heterojunction, which could ameliorate the separation efficiency of carriers and accelerate the accumulation of photogenerated electrons on LDHs. (2) LDHs nanosheets act as an electron enrichment site and a shell of the catalyst, which is beneficial to the adsorption and activation of N_2. The experimental results show that Bi_2O_3@CoAl-LDHs exhibits significantly enhanced photocatalytic nitrogen fixation activity compared with pure hollow Bi_2O_3 and LDHs. The phase separation efficiency, interface migration efficiency and migration efficiency of surface photo-generated carriers in the photocatalyst are studied in detail by photoluminescence spectroscopy (PL), time-resolved photoluminescence spectroscopy (TRPL), transient photocurrent spectroscopy (Transient photocurrent response) and electrochemical impedance spectroscopy (EIS). In addition, density functional theory calculations (DFT) systematically dissect the formation mechanism of the electron transport path of Z-scheme mechanism and the active sites of the N_2 fixation reaction.

2. Experimental section

2.1. Materials

$Bi(NO_3)_3{\cdot}5H_2O$ (≥99.0%), glycerin (≥99.5%), $Co(NO_3)_2{\cdot}6H_2O$ (≥99.0%), $Al(NO_3)_3{\cdot}9H_2O$ (≥99.0%), Urea (≥99.5%) and NH_4F (≥98.0%) were obtained from Aladdin Chemical Reagent Co., Ltd. NaOH (98%) and Na_2CO_3 (99.5%) were purchased from Hangzhou Huadong Medicine Group Co, Ltd (China). All reagents were used without further purification.

2.2. Synthesis of hollow Bi_2O_3

3 mmol of $Bi(NO_3)_3{\cdot}5H_2O$ was dissolved in 20 mL mixed solution of ethanol and glycerol (the volume ratio of ethanol to glycerol was 1:1) and stirred for 10 min. Subsequently, the suspension was transferred to a 50 mL Teflon-lined stainless steel autoclave at 160 °C for 3 h. When the reaction was completed, the as-obtained precursor of Bi_2O_3 were collected by centrifugation, and then washed for several times with distilled water and ethanol. Finally, the precursor of Bi_2O_3 powder was calcined in air at 270 °C for 2 h (2 °C/min) to obtain hollow Bi_2O_3.

2.3. Synthesis of CoAl-LDHs

CoAl-LDHs was prepared by co-precipitation method. 60 mmol $Co(NO_3)_2{\cdot}6H_2O$ and 20 mmol $Al(NO_3)_3{\cdot}9H_2O$ were dispersed in 100 mL ultrapure water as solution A (n_{Co}/n_{Al} = 3:1). 80 mmol NaOH and 5 mmol Na_2CO_3 were dispersed in 100 mL ultrapure water as solution B. Solution A and B were added drop-by-drop into a 500 mL three-neck flask containing 50 mL ultrapure water and kept the pH at range of 9.0–9.2 with vigorous stirring. Subsequently, the reaction slurry was aged at 85 °C for 18 h. After that, the precipitate was collected by centrifugation (8000 rpm for 5 min) and washed with ultrapure water until reaching pH = 7. Finally, the LDH was obtained after drying at 80 °C for 24 h (noted as LDHs).

2.4. Synthesis of Bi_2O_3@CoAl-LDHs Z-scheme heterojunction photocatalysts

The synthesis process and structure diagram of Bi_2O_3@CoAl-LDHs photocatalysts are shown in Fig. 1a [25]. Amount of Bi_2O_3 (Bi_2O_3/Al^{3+} mole ratio = 0.5, 1, 2), 0.9 mmol $Co(NO_3)_3{\cdot}6H_2O$, 0.3 mmol $Al(NO_3)_3{\cdot}9H_2O$, 3 mmol urea, 1.2 mmol NH_4F were dispersed in 15 mL ultrapure water and ultrasonically dispersed for 15 min. After that, the obtained solution was moved to a 50 mL Teflon-lined stainless steel autoclave at 100 °C for 10 h. After cooling naturally to room temperature, the final product was isolated by centrifugation, washed with ultrapure water and ethanol several times, and vacuum dried at 80 °C overnight. The samples were denoted as BO@CA-0.5, BO@CA-1 and BO@CA-2, respectively. Note: the catalyst of BO@CA used in the following characterizations, pho-

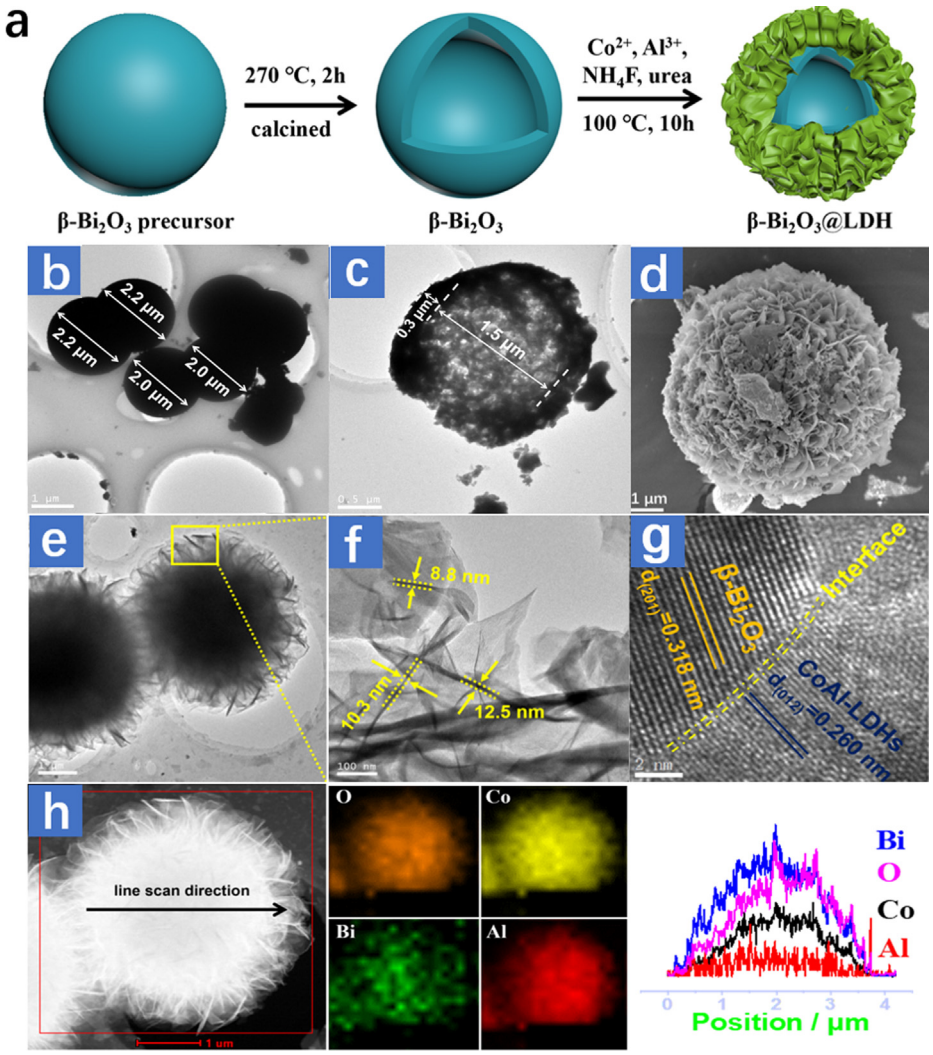

Fig. 1. Synthesis and characterization of BO@CA. Schematic illustration for synthetic route of BO@CA (a); TEM image of Bi_2O_3 precursor (b); TEM image of Bi_2O_3 (c); SEM image of BO@CA (d); TEM images of BO@CA (e and f). HRTEM image of BO@CA (g); Element mapping images and line scan of BO@CA (h). Note: Bi_2O_3@LDHs in picture *a* is shorten as BO@CA, BO@CA means BO@CA-1 catalyst.

tocatalytic nitrogen fixation or mechanism discussion means BO@CA-1.

2.5. Characterizations

The crystal structure was determined by X-ray diffractometer (XRD, Persee XD-6) with Cu Kα radiation (wavelength of 0.15418 nm) and the data were obtained in the 2θ range from 5° to 70°. The UV–vis diffuse reflection spectra (DRS) were recorded by Shimadzu-2600, with $BaSO_4$ as reflectance standard reference (the scanning range was 200–800 nm). The morphology of the photocatalysts were analyzed by scanning electron microscopy (SEM, Gemini 500) and transmission electron microscopy (TEM, Tecnai G2 F30, 300 kV). The catalyst surface compositions and valence band potential were measured by X-ray photoelectron spectroscopy (XPS, Thermo Fischer ESCALAB 250Xi, Al Kα, 12.5 kV, 16 mA, charge correction with C1s = 284.6 eV). The Photoluminescence (PL) spectra of the samples were analyzed on a Hitachi F-4600 fluorescence spectrometer at room temperature, and the excitation wavelength was 350 nm. A FS5 fluorescence lifetime spectra (Edinburgh Instruments) was used to measure the time-resolved transient PL decay curves of samples at an excitation wavelength of 325 nm. In the electron paramagnetic resonance (EPR) experiment, the electron paramagnetic resonance spectrometer (Bruker, A300) used 5,5-dimethyl-1-pyrroline *N*-oxide (DMPO) to capture the superoxide radical ($\cdot O_2^-$) and hydroxyl radical (·OH).

2.6. Photoelectrochemical measurements

Transient photocurrent and electrochemical impedance spectra of samples was performed via a Zahner PP211 using a standard three-electrode system. In the standard three-electrode system, a saturated calomel electrode (SCE) was utilized as reference electrode and platinum wires were counter electrode, and the electrolyte solution was 0.1 M Na_2SO_4 solution. To make a working electrode, catalyst powder was deposited on an indium tin oxide (ITO) substrate. In brief, 10 mg sample is added to 10 mL ethanol solution under ultrasonic for 30 min. Next it is coated on the prepared clean ITO glass and dried in an oven at 80 °C for 1 h. A 300 W xenon lamp was used as the light source. The illumination time interval was 20 s (the light is turned on for 20 s, and the light is off for 20 s).

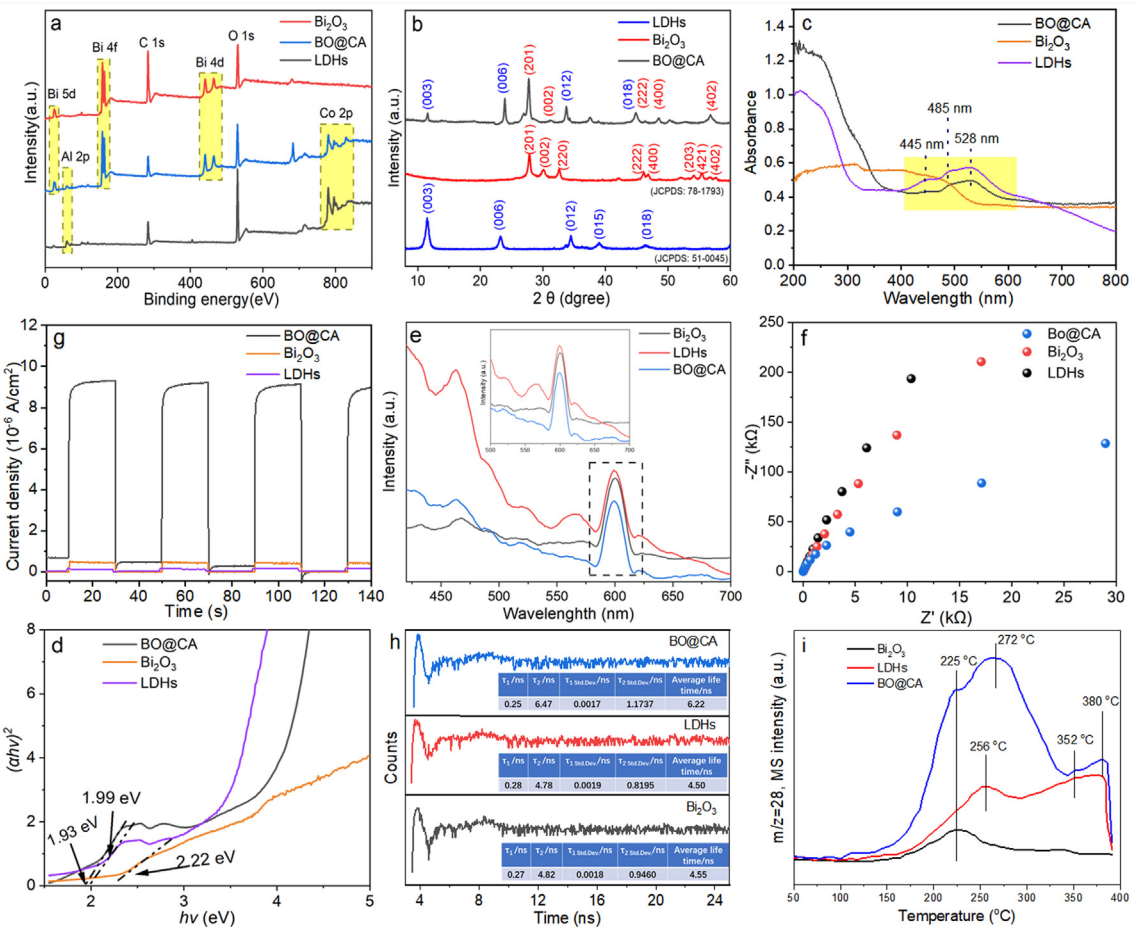

Fig. 2. Characterization of Bi_2O_3, LDHs and BO@CA photocatalysts: XPS survey (a); XRD patterns (b); UV–vis diffuse reflectance spectra (c) and plot of $(\alpha h\nu)^2$ versus $h\nu$ (d); Steady state fluorescence spectra (e); electrochemical impedance spectroscopy (EIS) Nyquist plots (f); Transient photocurrent response (g). Time-resolved PL spectra (h).N_2–TPD of Bi_2O_3, CoAl–LDHs and BO@CA samples (i). Note: BO@CA means BO@CA-1 catalyst.

2.7. Nitrogen photofixation reaction

The photocatalytic nitrogen fixation experiments were carried out at room temperature and in N_2 atmosphere. Typically, 50 mg of catalyst was dispersed in 150 mL of 0.25 M Na_2SO_3 solution (Na_2SO_3 was used as a sacrificial agent to consume photogenerated holes). The sample was sonicated to form uniform suspension, and then poured into a quartz reactor with pure N_2 (99.999%) bubbled at a flow rate of 200 mL/min^{-1} for 30 min in the dark. Subsequently, the reactor was sealed and irradiated under simulated visible light (with a cut off filter, $\lambda \geq 400$ nm) using a 300 W Xenon lamp (PL-X300D, 3.82 W/cm^2). After reaction, the concentration of ammonia ion (NH_4^+) in the reactor solution was detected using Nessler's reagent (standard curve of Nessler's reagent for detecting NH_4^+ is shown in Fig. S2) [26]. In brief, 10 mL of the reaction solution was collected with a syringe every 15 min and centrifuged immediately (8000 rpm, 10 min). Then, the centrifuged solution was filtered through a 0.22 μm filter into a 10 mL colorimetric tube. 200 μL of potassium sodium tartrate solution and 3000 μL of Nessler's reagent were added to the colorimetric tube one after another. After mixing for 15 min, the absorbance was measured at λ = 420 nm by Shimadzu UV-2600 spectrometer. Besides, the by-product hydrazine (N_2H_4) was detected by 4-dimethylaminobenzaldehyde reagent (Standard curve of 4-dimethylaminobenzaldehyde reagent for detecting N_2H_4 is shown in Fig. S3): the 10 mL reaction solution was taken out and centrifuged (8000 rpm, 10 min). The centrifuged solution was filtered through a 0.22 μm filter membrane into a 25 mL colorimetric tube, and 10 mL of p-dimethylaminobenzaldehyde solution was added. After mixing for 20 min, and then the absorbance was measured at λ = 458 nm by Shimadzu UV-2600 spectrometer [27].

2.8. Density functional theory calculations

Density functional theory (DFT) simulations were carried out based on the Cambridge Sequential Total Energy Package (CASTEP) [28]. Exchange-correlation energy was described by PerdueBurke-Ernzerhof (PBE) version of the generalized gradient approximation (GGA), and the projector augmented-wave (PAW) potential was used to represent the core-valence electron interaction [29]. An energy cutoff of 480 eV was used for the plane-wave expansion of the electronic wave function. Bi_2O_3 (100) crystal plane was built from the optimized Bi_2O_3 unit cell with lattice parameters of a = 7.738 Å, b = 7.738 Å, c = 5.731 Å, $\alpha = \beta = \gamma = 90°$ and the corresponding 1 × 1 × 1k-point mesh was modeled in the calculations (as displayed in Fig. S4). LDHs (003) crystal plane was built from the optimized CoAl-LDHs nanosheet unit cell with lattice parameters of a = 12.603 Å, b = 12.597 Å, c = 34.094 Å, $\alpha = \beta = 90°$, $\gamma = 119.83°$ and the corresponding 1 × 1 × 1 k-point mesh was modeled in the calculations (as displayed in Fig. S5). In addition, the heterostructure of Bi_2O_3 and LDHs was also constructed (as shown in Fig. S6). A vacuum region of about 20 Å was set to decouple the

periodic replicas in the calculations of LDHs (003) crystal plane and Bi_2O_3 (100) crystal plane. The force tolerance, total energy, maximum stress and maximum displacement for the relaxations were converged to 0.1 eV $Å^{-1}$, 5.0 × 10^{-5} eV/atom, 0.2 GPa and 0.005 Å, respectively.

3. Results and discussions

3.1. The morphology and element composition of the samples

The morphology and element composition of the samples can be analyzed by SEM, TEM, HRTEM and mapping characterization. As shown in Fig. 1b the morphology of the precursor of Bi_2O_3 is a solid sphere with a smooth surface and the diameter is ~2.1 μm. The TEM of Bi_2O_3 (Fig. 1c) shows that a hollow spherical structure with an outer layer of ~0.3 μm and an inner diameter of ~1.5 μm. As displayed in Fig. 1d and e, a 3D composite material with a flower-like surface and hollow spheres inside was synthesized after LDHs nanosheets were grown in situ on the surface of Bi_2O_3. Comparing with the solid structure, the internal hollow structure results in a shorter charge transfer path, which is beneficial to the migration of photogenerated carriers between Bi_2O_3 and LDHs [30,31]. In addition, the thickness of the LDHs nanosheets are ~10 nm (as shown in Fig. 1f), which is conducive to exposing active sites to to reduce N_2. The lattice spacing and two-phase interface can be observed in HRTEM image of BO@CA (Fig. 1g). The lattice spacing of 0.318 nm and 0.260 nm are correspond to the (201) crystal plane of Bi_2O_3 [32] and the (012) crystal plane of LDHs [33], respectively. It can also be clearly seen that Bi, O, Co, and Al are uniformly distributed in the selected area from the EDX mapping and line scan of BO@CA (Fig. 1h). In order to further analyze the element composition of the catalyst, Bi_2O_3, LDHs and BO@CA were characterized by XPS. As depicted in Fig. 2a, the elements of Bi, O, Co and Al appear in BO@CA, which is consistent with the analysis results of mapping.

The XRD pattern of pristine Bi_2O_3, LDHs and BO@CA are given in Fig. 2b. It can be seen that pristine Bi_2O_3 retain high crystallinity with diffraction peaks characteristic (JCPDS No.78-1793) of (201), (002), (220), (222), (400), (203), (421) and (402) [34]. The obvious characteristic diffraction peaks of (003), (006), (012), (015) and (018) crystal planes are shown in XRD pattern of LDHs, indicating that the sample is typical LDHs material (JCPDs No.51-0045) [35]. It is worth noting that the characteristic diffraction peaks of Bi_2O_3 and LDHs are appeared in XRD pattern of BO@CA. Thus, the results of TEM, XPS and XRD illustrates that the 3D core-shell BO@CA composite photocatalyst is successfully synthesized.

3.2. Optical and photoelectric properties

The photo-absorption properties is a key factor affecting photocatalytic performance. Therefore, the optical properties of samples was investigated by UV–vis DRS (Fig. 2c). LDHs has obvious absorption at visible light, and there are three absorption peaks at 445 nm, 485 nm and 528 nm. An interesting phenomenon is that the visible light absorption peaks similar to LDHs are appeared in BO@CA, impling the LDHs plays a key role in enhancing visible light absorption. Besides, The band gap (E_g) of Bi_2O_3, LDHs and BO@CA can be calculated by the Kubelka-Munk function: [36,37]

$$(\alpha h\upsilon) = A(h\upsilon - E_g)^{1/2} \quad (1)$$

where α, h, υ, A, and E_g are indicative to the absorption coefficient, Planck's constant, light frequency, constant value, and band gap, respectively. As shown in Fig. 2d, the band gaps of Bi_2O_3, LDHs

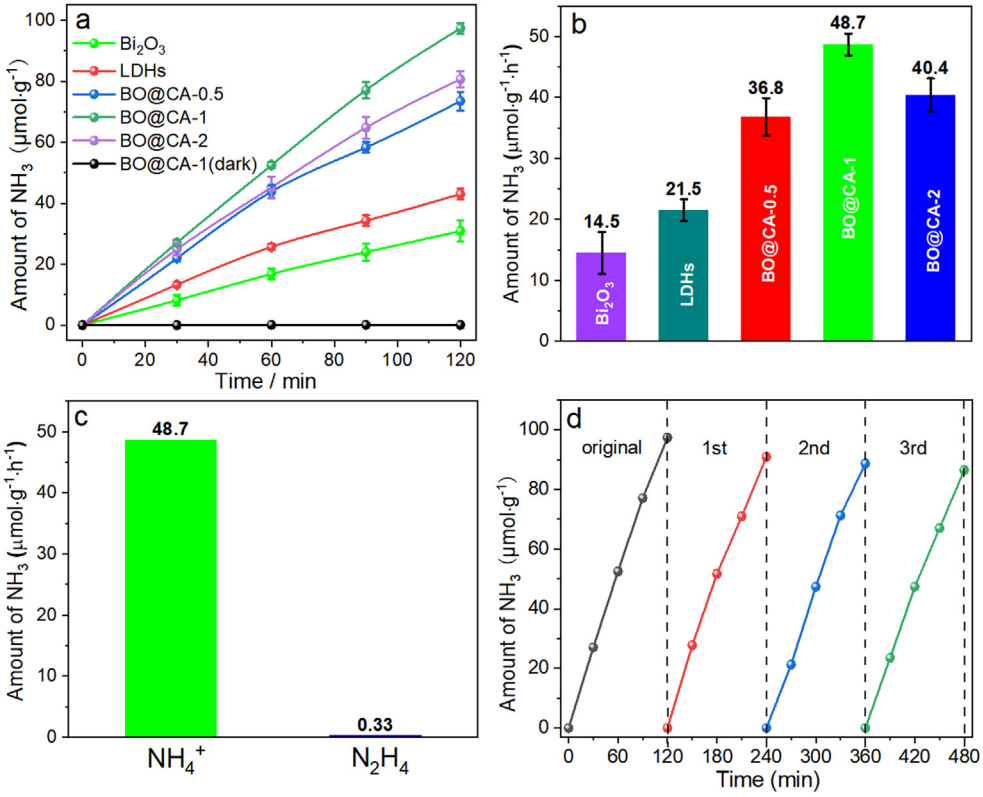

Fig. 3. Amount of NH_4^+ produced over different catalysts under the simulated visible-light irradiation (a); Production yield rates of ammonia over different photocatalysts (b); Comparison of the generation rate of NH_4^+ and N_2H_4 (c); Cycling runs for the visible light nitrogen fixation over BO@CA (d). Note: the catalyst used in picture *c* and *d* is BO@CA-1.

and BO@CA are 2.22 eV, 1.99 eV and 1.93 eV, respectively, suggesting that BO@CA is more likely to be excited by incident light to generate photo-generated carriers.

Photo-generated electron-hole pair separation and transfer efficiency is an another significant factor in evaluating photocatalytic performance. Therefore, a series of photoelectrochemical measurements were performed to investigate the separation and transfer efficiency of photo-generated carriers. Fig. 2e illustrates a comparison of the PL spectra for pure Bi_2O_3, LDHs and BO@CA. The PL intensity of the peaks decreases sharply after the heterojunction is formed between LDH and Bi_2O_3. This phenomenon indicates a significantly suppressed recombination of photogenerated charge carriers which benefits the electron-hole separation [38]. In addition, the EIS and the transient photocurrent response were performed to explore the photoelectric properties of the heterojunction interface. As shown in Fig. 2f, the EIS Nyquist radius of BO@CA is the smallest, indicating that BO@CA is more conducive to separation of carriers [39]. Meanwhile, BO@CA displays the largest photocurrent response value (Fig. 2g), revealing the higher separation efficiency of electron-hole pair [40]. It is also observed from the time-resolved fluorescence decay spectroscopy (TRPL, Fig. 2h), BO@CA exhibits a remarkably long average fluorescence lifetime (τ = 6.22 ns) with reference to Bi_2O_3 (4.55 ns) and LDHs (4.50 ns), which promotes the migration of photogenerated electrons from the interface to the active site [41]. Based on the results of photoelectrochemical characterizations, BO@CA has better visible light utilization, bulk electrons separation and interface electrons transfer efficiency, suggesting higher photocatalytic N_2 fixation performance.

Furthermore, the adsorption of N_2 molecules was mainly carried out through temperature programmed desorption (TPD). The results are shown in Fig. 2i. It can be found that when Bi_2O_3 and LDHs formed heterojunction composite (blue line in the figure), the adsorption of N_2 was obviously enhanced, and the adsorption peak shifted to a certain extent. The new adsorption peaks appear at 380 °C, which indicates that the complex effect between Bi_2O_3 and LDHs enhances the chemical adsorption between N_2 molecules and the catalyst.

3.3. Photocatalytic N_2 fixation performance and stability

In the experiments of photocatalytic nitrogen fixation, ultrapure water is used as the hydrogen source for ammonia synthesis, high-purity N_2 is used as the nitrogen source and Na_2SO_3 is used as a sacrificial agent to consume photogenerated holes [42,43]. The results of experiments are shown in Fig. 3a, from which we can see that BO@CA-1 exhibits best photocatalytic production of NH_4^+ reached yield (97.4 $\mu mol \cdot g^{-1}$) after 2 h of illumination (λ > 400 nm). Then, its solar-to-ammonia (STA) energy-conversion efficiency was also examined under AM 1.5G simulated sunlight [44]. After 1 h of light, a total of 0.215 μmol ammonia were evolved, so the STA value of BO@CA-1 was determined to be 0.0013% (shown in SI). All samples are active for N_2 fixation with the rates of NH_3 evolution following the order BO@CA-1 (48.7 $\mu mol \cdot g^{-1} \cdot h^{-1}$) > BO@CA-2 (40.4 $\mu mol \cdot g^{-1} \cdot h^{-1}$) > BO@CA-0.5 (36.8 $\mu mol \cdot g^{-1} \cdot h^{-1}$) > LDHs (21.5 $\mu mol \cdot g^{-1} \cdot h^{-1}$) > Bi_2O_3 (14.5 $\mu mol \cdot g^{-1} \cdot h^{-1}$) (Fig. 3b). In addition, we compared the photocatalytic nitrogen fixation activity and experimental conditions with those reported in other literatures. The results are listed in Table S1. It can be seen that the photocatalytic activity of nitrogen fixation catalyzed by BO@CA in this work has somewhat advantages compared with many mainstream photocatalysts. The higher reaction rate of composite catalyst possibly can be due to that the

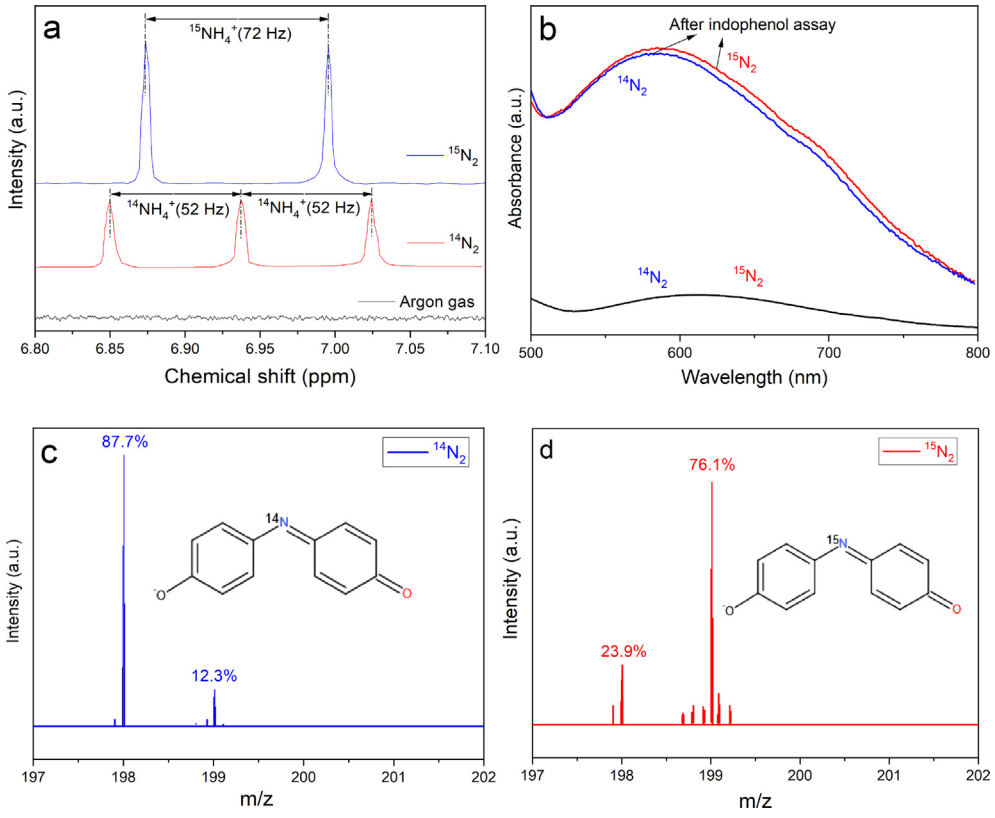

Fig. 4. The results of $^{15}N_2$ isotope labeling by NMR spectrum (a); UV–vis absorption spectra of the solutions from the nitrogen fixation reaction with $^{14}N_2$ or $^{15}N_2$ gas followed by the indophenol assay (b); mass spectra of the indophenol products obtained by reaction of phenol with ammonia generated from photocatalytic $^{14}N_2$ (c) or $^{15}N_2$ (d) reduction. Note: the catalyst used is BO@CA–1.

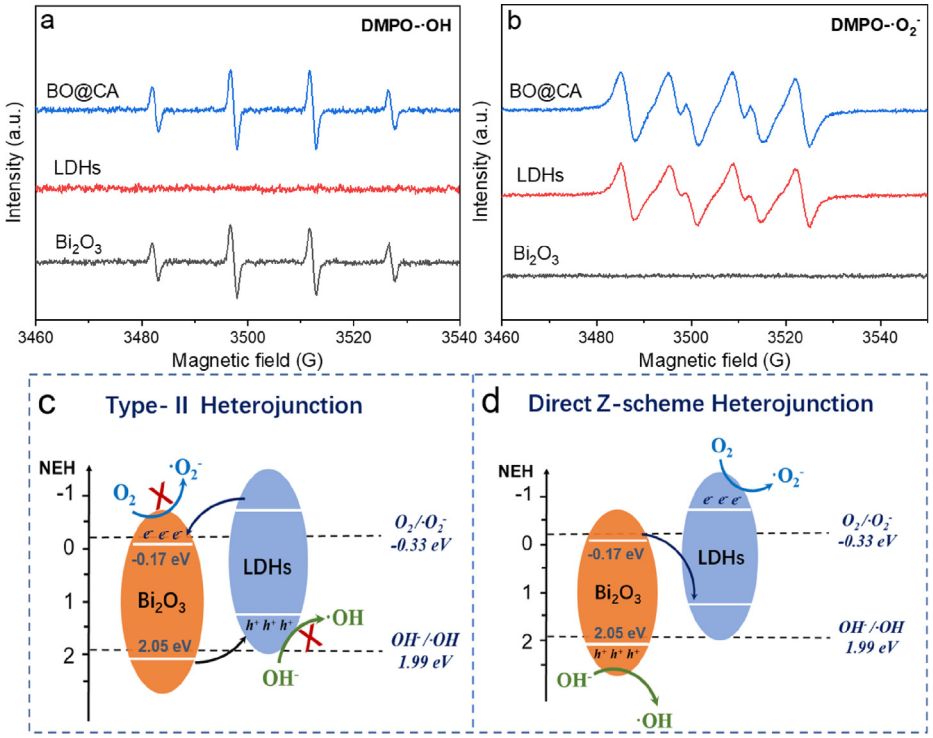

Fig. 5. EPR spectra of DMPO-·OH and DMPO-·O_2^- in the presence of Bi_2O_3, LDHs and BO@CA (a and b); Photocatalysis mechanism of Type II heterojunction (c) and direct Z-scheme heterojunction (d). Note: BO@CA means BO@CA-1 catalyst.

BO@CA Z-scheme heterojunction has photogenerated electrons with stronger oxidizing ability, better visible light utilization, bulk electrons separation and interface electrons transfer efficiency, which is consistent with the results of the photoelectric performance test of the samples (Fig. 2). In addition, the rate of by-product N_2H_4 evolution was detected in the photocatalytic N_2 fixation experiment catalyzed by BO@CA (Fig. 3c). The rate of NH_4^+ is about 147.6 times as much as the N_2H_4 (0.33 $\mu mol \cdot g^{-1} \cdot h^{-1}$), which indicates that the BO@CA composite photocatalyst exhibits excellent NH_4^+ selectivity. In addition, the photocatalytic N_2 fixation experiments were repeated three more times to assess the reusability and stability of the BO@CA (Fig. 3d). The cycling experiment illustrates that BO@CA still retains efficient photocatalysis after multiple runs. Besides, the SEM (Fig. S7) images reveal that the morphology of BO@CA remain unchanged after photocatalysis experiments, which collectively demonstrate that the prepared BO@CA exhibits excellent stability of structure and photocatalytic performance.

In order to confirm the accuracy of photocatalytic N_2 fixation, we took BA@CA–1 as the model catalyst to conduct strict control experiments (Fig. S8). When nitrogen was replaced by argon under visible light and nitrogen was used in ammonia synthesis under dark conditions, the amount of NH_3 can be ignored. Furthermore, in order to confirm that the hydrogen in the produced ammonia is from water, we used other solutions (dimethylformamide and acetonitrile) instead of water to carry out the experiment of pNRR under the same conditions (Fig. S8). It was found that the ammonia produced in the reaction solution of dimethylformamide (DMF) and acetonitrile can be ignored. This confirmed that N and H in NH_3 detected in this study came from N_2 photofixation rather than other nitrogen sources and water, respectively. In addition, $^{15}N_2$ was used for isotope labeling. When there is only argon in the reaction system, no signal appeared on the NMR spectrum (Fig. 4a). When $^{14}N_2$ items were introduced, because the spin of ^{14}N is one, the NMR spectrum of ^{14}N has three spin states (+1, 0 and −1), and its peak value is the triplet state with the coupling constant of 52 Hz [45]. When only $^{15}N_2$ item was introduced, the resonance spectrum splits into a double peak with a coupling constant of 72 Hz, because the spin of ^{15}N is 1/2, which indicates that it is spin-spin coupling [46]. Fig. 4b and d shows the UV–vis spectra and corresponding mass spectra of indophenol solutions from $^{14}N_2$ or $^{15}N_2$. There are two peaks at m/z = 198.05 and m/z = 199.05 in $^{14}N_2$ solution, which belong to indophenol anion. For $^{14}N_2$, the ratio of ^{14}N to ^{15}N is about 88/12 (Fig. 4c), while for $^{15}N_2$, the ratio of ^{14}N to ^{15}N is 24/76 (Fig. 4d). This further confirmed that the NH_3 detected in this study came from N_2 photofixation rather than other nitrogen sources.

4. Photocatalytic mechanism

4.1. Band arrangement of catalysts

In order to explore the photocatalytic N_2 fixation mechanism of BO@CA heterojunction photocatalyst, the energy band was analyzed. As shown in XPS-VB spectra (Fig. S9a), VB top of Bi_2O_3 and LDHs are 2.05 eV and 1.25 eV, respectively. The CB bottom can be calculated via using the Eq. (2): [47]

$$CB_{bottom} = VB_{top} - E_g \quad (2)$$

Thus, the CB bottoms of Bi_2O_3 and LDHs are –0.17 eV and –0.94 eV, respectively, indicating the energy bands show a cross arrangement (Fig. S9b). More significantly, the CB potential of the Bi_2O_3 and LDHs are more negative than the reduction potential of N_2/NH_3 (–0.0922 eV), suggesting that the photocatalytic N_2 fixation reaction is thermodynamically feasible.

4.2. Z-scheme electrons transfer mechanism and active site

We further discuss the Z–scheme electron transport mechanism by electron paramagnetic resonance (EPR) results. As shown in

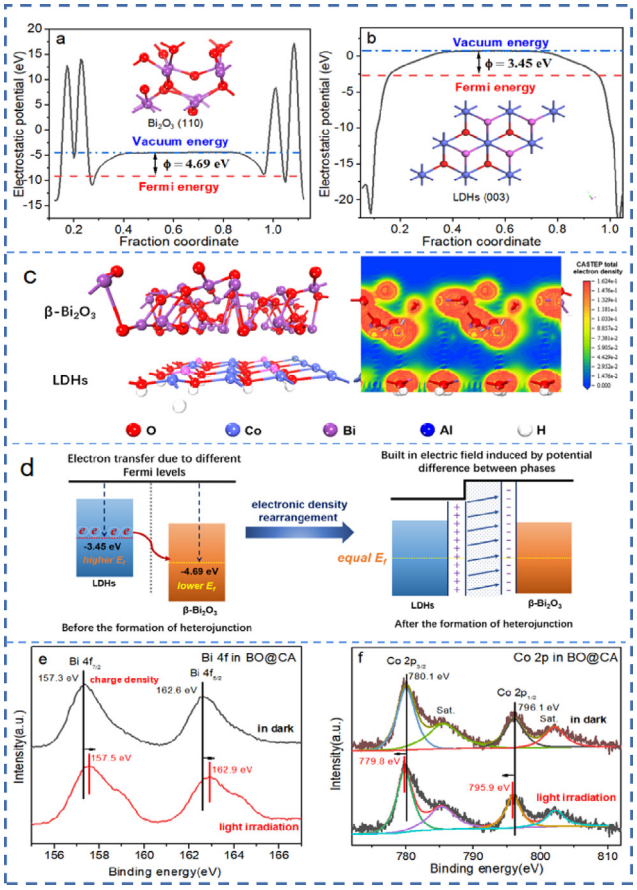

Fig. 6. Electrostatic potentials diagrams of Bi_2O_3 (a) and LDHs (b); The electron density distribution of BO@CA heterojunction (red represents negative charge, blue represents positive charge) (c); Schematic for the charge-transfer process and the formation of build-in electric field (BIEF) in BO@CA (d); in situ X–ray photoelectron spectroscopy results of Bi 4f (e) and Co 2p (f) for BO@CA sample under dark and light irradiation. Note: BO@CA means BO@CA–1 catalyst.

Fig. S10a and b, under dark conditions, there was no signal of DMPO–·OH and DMPO–$\cdot O_2^-$ for Bi_2O_3, LDHs and BO@CA–1. Under the condition of light (Fig. 5a and b), there is only DMPO–·OH signal, but no DMPO–$\cdot O_2^-$ signal in the EPR test results of Bi_2O_3. The valence band (hole) potential of Bi_2O_3 (2.05 eV) is higher than that of $OH^-/\cdot OH$ (1.99 eV), and the photogenerated electron potential (−0.17 eV) in conduction band is more positive than that of $O_2/\cdot O_2^-$ (−0.33 eV) [48]. Similarly, because the potential of hole in valence band (1.25 eV) of LDHs is lower than that of $OH^-/\cdot OH$, and the potential of photogenerated electron (−0.94 eV) on conduction band is more negative than that of $O_2/\cdot O_2^-$, only the signal of DMPO–$\cdot O_2^-$ and no signal of DMPO–·OH appears in EPR test results. In addition, it can be clearly seen that there are both signals of DMPO–·OH and DMPO–$\cdot O_2^-$ appeared in EPR result of BO@CA. That results indicate that the BO@CA composite retains the valence band (hole) of Bi_2O_3 with high oxidation ability, and also contains the conduction band of photogenerated electrons in LDHs with strong reduction ability. It also shows that the electron transfer between Bi_2O_3 and LDHs is not Type Ⅱ heterojunction, but Z–scheme heterojunction, that is, the photogenerated electrons transfer from the conduction band of Bi_2O_3 to the valence band of LDHs (Fig. 5c and d) [49,50].

Based on the characteristics that charges transfer from high Fermi energy to low Fermi energy during the formation of heterojunction (charges rearrangement process), the work function of Bi_2O_3 and LDHs can be calculated by using density functional theory (DFT), and then the Fermi energy of Bi_2O_3 and LDHs can be obtained according to formula (3): [51,52]

$$E_F = E_{vac} - j \tag{3}$$

where E_F, φ and E_{vac} represent Fermi energy, work function and vacuum energy (defined as 0 [53]), respectively.

The work function calculation results are shown in Fig. 6a and b. the work functions of Bi_2O_3 and LDHs are 4.69 eV and 3.35 eV, illustrating Fermi energy are −4.69 eV and −3.35 eV, respectively. It is obvious that E_F of LDHs is higher than Bi_2O_3. Therefore, the E_F difference between the Bi_2O_3 and LDHs promotes the charges transfer from LDHs to Bi_2O_3 until the E_F tends to be consistent.

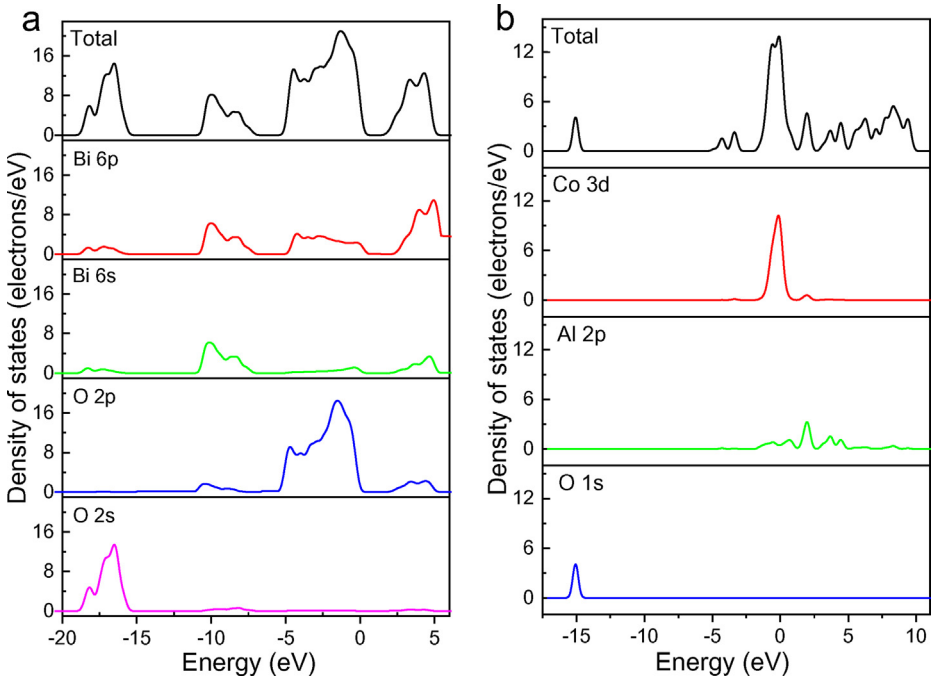

Fig. 7. The partial density of states (PDOS) for Bi_2O_3 (a) and LDHs (b).

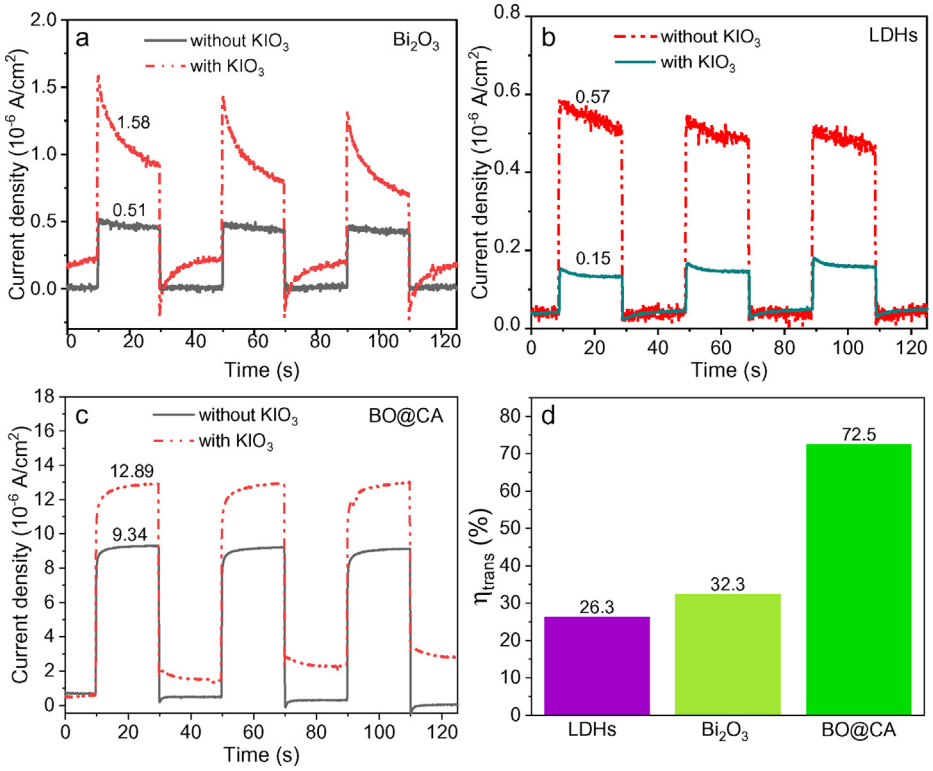

Fig. 8. Transient photocurrent response of (a) Bi_2O_3, LDHs (b) and BO@CA (c) with and without KIO_3 and the η_{trans} values calculated from surface electron transfer efficiency of LDHs, Bi_2O_3 and @BO@CA (d). Note: BO@CA means BO@CA–1 catalyst.

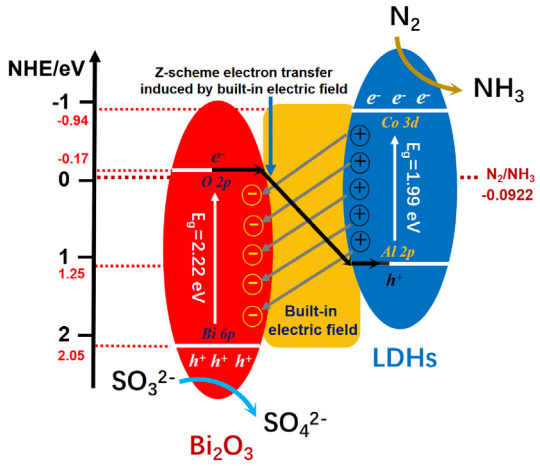

Fig. 9. Electron transfer mechanism of BO@CA Z-scheme heterojunction photocatalyst.

To further prove charge transfer between Bi_2O_3 and LDHs, the charge density of the BO@CA heterojunction can be calculated (Fig. 6c, red indicates negative charge and blue indicates positive charge). It is evident that the charges transfer from LDHs to Bi_2O_3 in heterojunction. The analysis of charge density further confirmed the existence of charges rearrangement process from LDHs to Bi_2O_3. The potential difference between Bi_2O_3 and LDHs is formed due to charge rearrangement of heterojunction between LDHs and Bi_2O_3, which promotes the formation of a built-in electric field (BIEF, the direction is LDHs → Bi_2O_3, as displayed in Fig. 6d). The BIEF could induce the migration direction of photogenerated electrons, which is opposite to the field strength of the built-in electric field. Therefore, Z-scheme electrons transfer mechanism is constructed that photogenerated electrons on the CB of Bi_2O_3 will migrate to VB of LDHs, with the result that the photo-generated electrons are mainly enriched on the CB of LDHs and the holes are mainly enriched on the VB of Bi_2O_3.

In addition, in order to further clarify whether the interfacial charge transfer between Bi_2O_3 and LDHs conforms to the Type II or direct Z–scheme heterojunction, the BO@CA sample was characterized by in situ X–ray photoelectron spectroscopy (Fig. 6e and f). In the absence of light, two peaks appear at 157.3 eV (Bi $4f_{7/2}$) and 162.6 eV (Bi $4f_{5/2}$) for BO@CA. The binding energy of Bi 4f has a slight positive shift (about 0.2 eV) under illumination, indicating that the electron density of Bi 4f decreases under irradiation (Fig. 6e). Meanwhile, two characteristic peaks at 780.1 (Co $2p_{3/2}$) and 796.1 eV (Co $2p_{1/2}$) were observed in the absence of light (Fig. 6f). The two peaks shifted negatively (about −0.2 eV) under illumination, indicating that the electron density of LDHs in the composite increased. The change of binding energy further confirmed the carrier migration path at the interface between Bi_2O_3 and LDHs under irradiation [54]. More precisely, photogenerated electrons migrate from Bi_2O_3 to LDHs, which is consistent with the mechanism of direct Z–scheme heterojunction.

Z–scheme electron transport path in BO@CA photocatalyst was confirmed by EPR and DFT calculation, that is, the transfer of photogenerated electrons from the conduction band of Bi_2O_3 to the valence band of LDHs. In other words, the reduction reaction takes place in the conduction band of LDHs, while the oxidation reaction takes place in the valence band of Bi_2O_3. Because the conversion of N_2 to NH_3 is a reduction reaction, the conduction band of LDHs is the site of photocatalytic nitrogen fixation. According to the reference that the active sites can be inferred by analyzing the energy band composition of the catalyst [55,56]. As shown in Fig. 7a, for the VB of Bi_2O_3 is mainly composed of 2p orbitals with Bi element, while CB is mainly composed of 2p of O. In addition, VB of LDHs is mainly composed of 2p orbitals with Al element, while CB is

mainly composed of 3d of Co (Fig. 7b). According to the Z-scheme electrons transfer mechanism, it can be inferred that the photogenerated electrons transfer from the O 2p orbital to the Al 2p orbital. Notably, the photogenerated electrons involved in photocatalytic N_2 fixation accumulate on the CB of LDHs (Co 3d orbital), suggesting Co element is the active site for photocatalytic reaction. In addition, the process of ammonia synthesis from nitrogen catalyzed by BO@CA was further simulated and discussed. It is found that N_2 is more likely to be adsorbed on the Co–top site (Fig. S11b and c). Thus, combined with the above discusses, it can be inferred that Co is the active site of photocatalytic nitrogen fixation.

4.3. Z-scheme heterojunction promotes the transfer efficiency of photogenerated carriers

Based on the transient photocurrent test, the fast photogenerated electron scavenger KIO_3 was added in the electrolyte to further investigate the promoting effect of the BIEF on the transfer efficiency of surface photogenerated carriers (η_{trans}). The $\eta_{trans}$of the samples can be obtained by comparing the photocurrent with and without the addition of the KIO_3 (1 mM) in the electrolyte. The relationship between photocurrent and η_{trans} is as follows: [57]

$$J_{water} = J_{max} \cdot \eta_{abs} \cdot \eta_{sep} \cdot \eta_{trans} \quad (4)$$

$J_{water}$and J_{max}represent for the measured and the theoretical maximum photocurrent without electrons scavenger, respectively; η_{abs}, η_{sep} and η_{trans} represent the light absorption efficiency, photogenerated carriers separation efficiency and transfer efficiency of photogenerated surface carriers, respectively.

When KIO_3 is added to the solution, η_{trans} is close to 100%:

$$J_{KIO_3} = J_{max} \cdot \eta_{abs} \cdot \eta_{sep} \cdot 100\% \quad (5)$$

Thus, η_{trans}can be calculated by formula (6): [58]

$$\eta_{trans} = \frac{J_{KIO_3}}{J_{water}} \times 100\% \quad (6)$$

where J_{KIO_3} is the maximum photocurrent value detected when KIO_3 is added.

As shown in Fig. 8a and b, the photocurrent density of Bi_2O_3 is increased from 0.51 μA cm^{-2} to 1.58 μA cm^{-2} and the photocurrent density of LDHs is increased from 0.15 μA cm^{-2} to 0.57 μA cm^{-2} after adding KIO_3. However, the photocurrent density of BO@CA is increased from 9.34 μA cm^{-2} to 12.89 μA cm^{-2} (Fig. 8c). As shown in Fig. 8d, the $\eta_{trans}$is determined to be 26.3%, 32.3% and 72.5% for LDHs, Bi_2O_3 and BO@CA, respectively, validating transfer efficiency of surface electrons promoted by fabrication of Z-scheme heterojunction, which contributes to the enhanced photocatalytic N_2 fixation performance.

4.4. Mechanism of photocatalytic N_2 fixation of Bi_2O_3@CoAl-LDHs Z-scheme heterojunction

Based on above results, a photocatalytic N_2 fixation mechanism of BO@CA direct Z-scheme heterojunction is proposed and as shown in Fig. 9: (1) The band gaps of Bi_2O_3 and LDHs are 2.22 eV and 1.99 eV, respectively. Thus, photogenerated electrons and holes will be generated when excited by visible light, that is, photogenerated electrons are accumulated on the CB and photogenerated holes are accumulated on the VB. (2) The photogenerated electrons on the CB of LDHs will transfer to the VB of Bi_2O_3 and recombine with holes via the induction of the BIEF. Photogenerated electrons with more negative potentials and holes with more positive potentials are accumulated on the CB of LDHs (Co 3d) and VB of Bi_2O_3 (Bi 6p), respectively, which implies that Co is the active site for the photocatalytic N_2 fixation reaction. More importantly, the BIEF can greatly enhance average lifetime (6.22 ns) and surface transfer efficiency of photogenerated electrons (72.5%). (3) Na_2SO_3 as a scavenger can quickly capture holes in the Bi_2O_3 valence band, while LDHs nanosheets as enrichment sites of photogenerated electrons and shell structure can effectively capture N_2 to generate NH_4^+.

5. Conclusion

In summary, a 3D hollow Bi_2O_3@CoAl-LDHs (BO@CA) direct Z-scheme heterojunction photocatalyst was synthesized and used for photocatalytic N_2 fixation. The prepared BO@CA-1 heterojunction possesses enviable photocatalytic NH_3 evolution property with capability to generate NH_3 rate up to 48.7 μmol $h^{-1}.g^{-1}$. The improved photocatalytic performance arises from the fact that Z-scheme heterojunction with larger contact area and strong electron coupling effect stimulate photogenerated charge kinetics. Notably, the surface migration efficiency of photogenerated electrons in the Z-scheme heterojunction has been tested pioneeringly (72.5%). Furthermore, this work reveals that the BIEF between Bi_2O_3 and LDHs is the key to inducing the formation of a Z-scheme heterojunction where the photogenerated electrons are transferred from the O 2p orbital to the Al 2p orbital. Our approach may also be potentially to activate other 3D core-shell Z-scheme heterojunction systems for high photocatalytic N_2 fixation.

CRediT authorship contribution statement

Shengjie Xia: Writing - original draft, Investigation, Supervision, Project administration. **Guanhua Zhang:** Writing - original draft, Data curation. **Zhiyan Gao:** Data curation, Writing - review & editing, Visualization. **Yue Meng:** Data curation, Writing - review & editing, Visualization. **Bo Xie:** Visualization, Writing - review & editing, Project administration. **Hanfeng Lu:** Data curation, Software, Validation. **Zheming Ni:** Data curation, Software, Validation.

Declaration of Competing Interest

The authors declare that they have no known competing financial interests or personal relationships that could have appeared to influence the work reported in this paper.

Acknowledgment

This work is supported by National Natural Science Foundation of China (92061126, 51871091, 21503188).

Appendix A. Supplementary material

Supplementary data to this article can be found online at https://doi.org/10.1016/j.jcis.2021.07.063.

References

[1] T. Rayment, R. Schlogl, J. Thomas, G. Ertl, Structure of the ammonia synthesis catalyst, Nature 315 (1985) 311–313.
[2] L. Wang, M.K. Xia, H. Wang, K.F. Huang, C.X. Qian, C.T. Maravelias, G.A. Ozin, Greening ammonia toward the solar ammonia refinery, Joule 2 (2018) 1055–1074.
[3] J.Z. Qin, B.J. Liu, K.H. Lam, S.J. Song, X.Y. Li, X. Hu, 0D/2D MXene quantum dot/Ni-MOF ultrathin nanosheets for enhanced N-2 photoreduction, ACS Sustainable Chem. Eng. 8 (2020) 17791–17799.
[4] J.P. Guo, P. Chen, Catalyst: NH_3 as an energy carrier, Chem 3 (2017) 709–712.
[5] G.N. Schrauzer, T.D. Guth, Photolysis of water and photoreduction of nitrogen on titanium dioxide, J. Am. Chem. Soc. 99 (1977) 7189–7193.

[6] R. Shi, Y. Zhao, G.I.N. Waterhouse, S. Zhang, T. Zhang, Defect engineering in photocatalytic nitrogen fixation, ACS Catal. 9 (2019) 9739–9750.

[7] J.Z. Qin, W.J. Zhao, X. Hu, J. Li, P. Ndokoye, B.J. Liu, Exploring the N-2 adsorption and activation mechanisms over the 2H/1T mixed-phase ultrathin Mo1-xWxS2 nanosheets for boosting N-2 photosynthesis, ACS Appl. Mater. Interfaces 13 (2021) 7127–7134.

[8] S. Bian, M. Wen, J.H. Wang, N. Yang, P.K. Chu, X.F. Yu, Edge-rich black phosphorus fo-r photocatalytic nitrogen fixation, J. Phys. Chem. Lett. 11 (2020) 1052–1058.

[9] G.H. Zhang, T.T. Dai, Y. Wang, Y. Meng, B. Xie, Z.M. Ni, S.J. Xia, Modulation of photo-generated solvated electrons for ammonia synthesis via facet-dependent engineering of heterojunctions, Appl. Catal. B 288 (2021) 119990.

[10] Y.X. Zhao, L.R. Zheng, R. Shi, S. Zhang, X.A. Bian, F. Wu, X.Z. Cao, G.I.N. Waterhouse, T.R. Zhang, Alkali etching of layered double hydroxide nanosheets for enhanced photocatalytic N_2 reduction to NH_3, Adv. Energy Mater. 10 (2020) 2002199.

[11] G.H. Zhang, X.Q. Zhang, Y. Meng, G.X. Pan, Z.M. Ni, S.J. Xia, Layered double hydroxides-based photocatalysts and visible-light driven photodegradation of organic pollutants: A review, Chem. Eng. J. 392 (2020) 123684–123710.

[12] G.H. Zhang, X.F. Zhang, Y. Meng, X.B. Zhou, G.X. Pan, Z.M. Ni, S.J. Xia, Experimental and theoretical investigation into visible-light-promoted selective hydrogenation of crotonaldehyde to crotonyl alcohol using Au-Co, Ni alloy nanoparticle supported layered double hydroxides, J. Mater. Chem. A 6 (2018) 15839–15852.

[13] Y.F. Zhao, Y.X. Zhao, G.I.N. Waterhouse, L.R. Zheng, X.Z. Cao, F. Teng, L.Z. Wu, C. H. Tung, D. O'Hare, T.R. Zhang, Layered-double-hydroxide nanosheets as efficient visible-light-driven photocatalysts for dinitrogen fixation, Adv. Mater. 29 (2017) 1703828.

[14] B. Song, Z.T. Zeng, G.M. Zeng, J.L. Gong, R. Xiao, S.J. Ye, M. Chen, C. Lai, P. Xu, X. Tang, Powerful combination of g-C_3N_4 and LDHs for enhanced photocatalytic performance: a review of strategy, synthesis, and applications, Adv. Colloid. Interf. 272 (2019) 101999–102015.

[15] S.J. Xia, G.H. Zhang, Y. Meng, C. Yang, Z.M. Ni, J. Hu, Kinetic and mechanistic analysis for the photodegradation of gaseous formaldehyde by core-shell CeO_2@LDHs, Appl. Catal. B 278 (2020) 119266.

[16] Z. Zhong, J.J. Liu, X. Xu, A.H. Cao, Z.J. Tao, W.F. You, L.T. Kang, Synthesis of Z-scheme cobalt porphyrin/nitrogen-doped graphene quantum dot heterojunctions for efficient molecule-based photocatalytic oxygen evolution, J. Mater. Chem. A 9 (2021) 2404–2413.

[17] H.D. Tang, W.J. Zhang, Y. Meng, S.J. Xia, A direct Z-scheme heterojunction with boosted transportation of photogenerated charge carriers for highly efficient photodegradation of PFOA: Reaction kinetics and mechanism, Appl. Catal. B 285 (2021) 119851.

[18] V.H. Nguyen, M. Mousavi, J.B. Ghasemi, Q.V. Le, S.A. Delbari, M.S. Asl, M. Shokouhimehr, M. Mohammadi, Y. Azizian-Kalandaragh, A.S. Namini, In situ preparation of g-C3N4 nanosheet/FeOCl: achievement and promoted photocatalytic nitrogen fixation activity, 587 (2021) 538–549.

[19] X.W. Feng, H. Chen, F. Jiang, X. Wang, In-situ self-sacrificial fabrication of lanthanide hydroxycarbonates/graphitic carbon nitride heterojunctions: nitrogen photofixation under simulated solar light irradiation, Chem. Eng. J. 347 (2018) 849–859.

[20] X.Y. Yang, Y.M. Zhang, Y.L. Wang, C.L. Xin, P. Zhang, D. Liu, B.B. Mamba, K.K. Kefeni, A.T. Kuvarega, J.Z. Gui, Hollow β-Bi_2O_3@CeO_2 heterostructure microsphere with controllable crystal phase for efficient photocatalysis, Chem. Eng. J. 387 (2020) 124100.

[21] H. Wang, L. Zhang, Z. Chen, J. Hu, S. Li, Z. Wang, J. Liu, X. Wang, Semiconductor heterojunction photocatalysts: design, construction, and photocatalytic performances, Chem. Soc. Rev. 43 (2014) 5234–5244.

[22] X.Y. Liu, Z. Yang, L. Zhang, In-situ fabrication of 3D hierarchical flower-like β-Bi_2O_3@CoO Z-scheme heterojunction for visible-driven simultaneous degradation of multi-pollutants, J. Hazard. Mater. 403 (2021) 123566.

[23] Y.L. Lan, Z.S. Li, D.H. Li, W.Y. Xie, G.X. Yan, S.H. Guo, Visible-light responsive Z-scheme Bi@β-Bi_2O_3/g-C_3N_4 heterojunction for efficient photocatalytic degradation of 2,3-dihydroxynaphthalene, Chem. Eng. J. 392 (2020) 123686.

[24] Y.J. Pang, Y.W. Li, G.Q. Xu, Y.T. Hu, Z.K. Kou, Q. Feng, J. Lv, Y. Zhang, J. Wang, Y.C. Wu, Z-scheme carbon-bridged Bi_2O_3/TiO_2 nanotube arrays to boost photoelectrochemical detection performance, Appl. Catal. B 248 (2019) 255–263.

[25] A. Ziarati, A. Badiei, R. Grillo, T. Burgi, 3D Yolk@Shell TiO_{2-x}/LDH Architecture: Tailored Structure for Visible Light CO_2 Conversion, ACS Appl. Mater. Interfaces 11 (2019) 5903–5910.

[26] S.H. Cao, N. Zhou, F.H. Gao, H. Chen, F. Jiang, All-solid-state Z-scheme 3,4-dihydroxybenzaldehyde-functionalized Ga_2O_3/graphitic carbon nitride photocatalyst with aromatic rings as electron mediators for visible-light photocatalytic nitrogen fixation, Appl. Catal. B 218 (2017) 600–610.

[27] X. Chen, Y.F. Li, Z.S. Wu, X.L. Xu, W. Zhu, X.M. Gao, Bi_4O_5Br 2 anchored on T_i3_C2 MXene with ohmic heterojunction in photocatalytic N_H3 production: Insights from combined experimental and theoretical calculations, J. Colloid Interf. Sci. 602 (2021) 553–562.

[28] Y. Meng, Y.F. Chen, X.B. Zhou, G.X. Pan, S.J. Xia, Experimental and theoretical investigations into the activity and mechanism of water–gas shift reaction catalyzed by Au nanoparticles supported on Zn–Al/Cr/Fe layered double hydroxides, Int. J. Hydrogen Energ. 45 (2020) 464–476.

[29] Y. Wang, Y. Meng, Z.M. Ni, S.J. Xia, Promotion of H_2 adsorption performance on InN monolayer by embedding Cu atom: a first-principles study, Int. J. Hydrogen Energ. 46 (2021) 848–857.

[30] L.L. Zhang, Y.L. Shi, Z.Q. Wang, C. Hu, B.Y. Shi, X.Z. Cao, Porous β-Bi2O3 with multiple vacancy associates on highly exposed active 220 facets for enhanced photocatalytic activity, Appl. Catal. B 265 (2020) 118563.

[31] S.B. Wang, Y. Wang, S.Q. Zang, X.W. Lou, Hierarchical Hollow Heterostructures for Photocatalytic CO_2 Reduction and Water Splitting, Small Methods 4 (2019) 1900586.

[32] B.B. Shao, Z.F. Liu, G.M. Zeng, Y. Liu, Q.H. Liang, Q.Y. He, T. Wu, Y. Pan, J. Huang, Z. Peng, S.H. Luo, C. Liang, X.J. Liu, S.H. Tong, J. Liang, Synthesis of 2D/2D CoAl-LDHs/$Ti_3C_2T_x$ Schottky-junction with enhanced interfacial charge transfer and visible-light photocatalytic performance, Appl. Catal. B 286 (2021) 119867.

[33] H. Guo, C.G. Niu, X.J. Wen, L. Zhang, C. Liang, X.G. Zhang, D.L. Guan, N. Tang, G. M. Zeng, Construction of highly efficient and stable ternary AgBr/Ag/$PbBiO_2Br$ Z-scheme photocatalyst under visible light irradiation: performance and mechanism insight, J. Colloid Interf. Sci. 513 (2018) 852–865.

[34] D.B. Wang, X. Yu, Q.G. Feng, X.H. Lin, Y. Huang, X.Q. Huang, X. Li, K. Chen, B.H. Zhao, Z. Zhang, β-Bi_2O_3 nanosheets on g-C_3N_4 to construct direct Z-scheme heterojunction with enhanced photocatalytic activities, J. Alloy. Compd. 859 (2021) 157795.

[35] W.N. Yang, J. Lia, M. Liu, D.H.L. Ng, Y. Liu, X.F. Sun, J. Yang, Bioinspired hierarchical CoAl-LDH/MFe_2O_4 (Ni, Zn, Co) as peroxidase mimics for colorimetric detection of glucose, Appl. Clay Sci. 181 (2019) 10523.

[36] C. Yang, G.H. Zhang, Y. Meng, G.X. Pan, Z.M. Ni, S.J. Xia, Direct Z-scheme CeO_2@LDH core–shell heterostructure for photodegradation of Rhodamine B by synergistic persulfate activation, J. Hazard. Mater. 408 (2021) 124908.

[37] H.T. Zhao, L.Y. Guo, C.W. Xing, H.Y. Liu, X.Y. Li, A homojunction–heterojunction–homojunction scaffold boosts photocatalytic H_2 evolution over $Cd_{0.5}Zn_{0.5}S$/CoO hybrids, J. Mater. Chem. A 8 (2020) 1955–1965.

[38] P.F. Tan, Y. Liu, A.Q. Zhu, W.X. Zeng, H. Cui, Ju. Pan, Rational design of Z-scheme system based on 3D hierarchical CdS supported 0D Co_9S_8 nanoparticles for superior photocatalytic H_2 generation, ACS Sustainable Chem. Eng. 6 (2018) 10385–10394.

[39] L.B. Wang, Q. Zhang, T.T. Wei, F.Y. Li, Z.X. Sun, L. Xu, WC and cobalt nanoparticles embedded in nitrogen-doped carbon 3D nanocage derived from $H_3PW_{12}O_{40}$@ZIF-67 for photocatalytic nitrogen fixation, J. Mater. Chem. A 9 (2021) 2912–2918.

[40] J. Li, Q. Pei, R.Y. Wang, Y. Zhou, Z.M. Zhang, Q.Q. Cao, D.H. Wang, W.B. Mi, Y.W. Du, Enhanced photocatalytic performance through magnetic field boosting carrier transport, ACS Nano 12 (2018) 3351–3359.

[41] K.H. Ye, Y. Li, H. Yang, M.Y. Li, Y.C. Huang, S.Q. Zhang, H.B. Ji, An ultrathin carbon layer activated CeO_2 heterojunction nanorods for photocatalytic degradation of organic pollutants, Appl. Catal. B 259 (2019) 118085.

[42] N. Zhang, A. Jalil, D. Wu, S. Chen, Y. Liu, C. Gao, W. Ye, Z. Qi, H. Ju, C. Wang, Refining defect states in $W_{18}O_{49}$ by Mo doping: a strategy for tuning N_2 activation towards solar-driven nitrogen fixation, J. Am. Chem. Soc. 140 (2018) 9434–9443.

[43] S.W. Zhang, H.C. Yang, H.H. Gao, R.Y. Cao, J.Z. Huang, X. Xu, One-pot synthesis of CdS irregular nanospheres hybridized with oxygen-incorporated defect-rich MoS_2 ultrathin nanosheets for efficient photocatalytic hydrogen evolution, ACS Appl. Mater. Interfaces 9 (2017) 23635–23646.

[44] J.L. Yuan, X.Y. Yi, Y.H. Tang, M.J. Liu, C.B. Liu, Efficient photocatalytic nitrogen fixation: enhanced polarization, activation, and cleavage by asymmetrical electron donation to N≡N bond, Adv. Funct. Mater. 30 (2019) 1906983.

[45] A.C. Nielander, J.M. McEnaney, J.A. Schwalbe, J.G. Baker, S.J. Blair, L. Wang, J.G. Pelton, S.Z. Andersen, K.E. Rasmussen, V. Čolić, S. Yang, S.F. Bent, M. Cargnello, J. Kibsgaard, P.C.K. Vesborg, I. Chorkendorff, T.F. Jaramillo, A versatile method for ammonia detection in a range of relevant electrolytes via direct nuclear magnetic resonance techniques, ACS Catal. 9 (2019) 5797–5802.

[46] Z. Zhao, D.D. Wang, R. Gao, G.B. Wen, M. Feng, G.X. Song, J.B. Zhu, D. Luo, H.Q. Tan, X. Ge, W. Zhang, Y.J. Zhang, L.R. Zheng, H.B. Li, Z.W. Chen, Magnetic-field-stimulated efficient photocatalytic N_2 fixation over defective $BaTiO_3$ perovskites, Angew. Chem. Int. Ed. 60 (2021) 11910–11918.

[47] X.H. Li, Z.X. Yu, L.Y. Shao, H.J. Zeng, Y.C. Liu, X.F. Feng, A novel strategy to construct a visible–light–driven Z–scheme (ZnAl–LDH with active phase/g–C_3N_4) heterojunction catalyst via polydopamine bridge (a similar "bridge" structure), J. Hazard. Mater. 386 (2020) 121650.

[48] B.F. Li, W.J. Wang, J.W. Zhao, Z.Y. Wang, B. Su, Y.D. Hou, Z.X. Ding, W.J. Ong, Sibo Wang, All-solid-state direct Z-scheme $NiTiO_3$/$Cd_{0.5}Zn_{0.5}S$ heterostructures for photocatalytic hydrogen evolution with visible light, J. Mater. Chem. A 9 (2021) 10270–10276.

[49] J.W. Fu, Q.L. Xu, J.X. Low, C.J. Jiang, J.G. Yu, Ultrathin 2D/2D WO3/g-C3N4 step-scheme H2-production photocatalyst, Appl. Catal. B 243 (2019) 556–565.

[50] Y.L. Wang, Y. Tian, Z.L. Lang, W. Guan, L.K. Yan, A highly efficient Z-scheme B-doped g-C_3N_4/SnS_2 photocatalyst for CO_2 reduction reaction: a computational study, J. Mater. Chem. A 6 (2018) 21056–21063.

[51] G.H. Zhang, Y. Meng, B. Xie, Z.M. Ni, H.F. Lu, Shengjie Xia, Precise location and regulation of active sites for highly efficient photocatalytic synthesis of ammonia by facet-dependent $BiVO_4$ single crystals, Appl. Catal. B 296 (2021) 120379.

[52] G.H. Zhang, T.T. Dai, Y. Meng, L.Y. Zhang, G.X. Pan, C. Yang, Z.M. Ni, S.J. Xia, Bridged-Au Z-scheme heterojunction ZnO-Au-$ZnAl_2O_4$: electron transfer and kinetics of photodegradation, Appl. Surf. Sci. 532 (2020) 147456.

[53] J. Liu, X.C. Zhang, Q. Zhong, J. Li, H.Z. Wu, B. Zhang, L. Jin, H.B. Tao, Bin Liu, Electrostatic self-assembly of a AgI/$Bi_2Ga_4O_9$ p–n junction photocatalyst for boosting superoxide radical generation, J. Mater. Chem. A 8 (2020) 4083–4090.

[54] Y.B. Dou, S.T. Zhang, T. Pan, S.M. Xu, A.W. Zhou, M. Pu, H. Yan, J.B. Han, M. Wei, D.G. Evans, X. Duan, TiO_2@layered double hydroxide core-shell nanospheres

with largely enhanced photocatalytic activity toward O_2 generation, Adv. Funct. Mater. 25 (2015) 2243–2249.
[55] Z.L. Wang, S.M. Xu, Y.Q. Xu, L. Tan, X. Wang, Y.F. Zhao, H.H. Duan, Y.F. Song, Single Ru atoms with precise coordination on a monolayer layered double hydroxide for efficient electrooxidation catalysis, Chem. Sci. 10 (2019) 378.
[56] L. Wang, J.X. Liu, W.Y. Song, H. Wang, Y. Li, J. Liu, Z. Zhao, J.B. Tan, Z.C. Duan, J.L. Deng, Experimental and DFT insights of $BiVO_4$ as an effective photocatalytic catalyst for N_2O decomposition, Chem. Eng. J. 366 (2019) 504–513.
[57] S. Jin, X.X. Ma, J. Pan, C.Y. Zhu, S.E. Saji, J.G. Hu, X.Y. Xu, L.T. Sun, Z.Y. Yin, Oxygen vacancies activating surface reactivity to favor charge separation and transfer in nanoporous $BiVO_4$ photoanodes, Appl. Catal. B 281 (2021) 119477.
[58] M. Li, S.X. Yu, H.W. Huang, X.W. Li, Y.B. Feng, C. Wang, Y.G. Wang, T.Y. Ma, L. Guo, Y.H. Zhang, Unprecedented eighteen-faceted BiOCl with a ternary facet junction boosting cascade charge flow and photo-redox, Angew. Chem. Int. Ed. 131 (2019) 9617–9621.